Computational investigation of surface freezing in a molecular model of water

Amir Haji-Akbari (امیر حاجی اکبری)[a,1] and Pablo G. Debenedetti[a,2]

[a]Department of Chemical and Biological Engineering, Princeton University, Princeton, NJ 08544

Contributed by Pablo G. Debenedetti, February 17, 2017 (sent for review December 21, 2016; reviewed by Christoph Dellago and Angelos Michaelides)

Water freezes in a wide variety of low-temperature environments, from meteors and atmospheric clouds to soil and biological cells. In nature, ice usually nucleates at or near interfaces, because homogenous nucleation in the bulk can only be observed at deep supercoolings. Although the effect of proximal surfaces on freezing has been extensively studied, major gaps in understanding remain regarding freezing near vapor–liquid interfaces, with earlier experimental studies being mostly inconclusive. The question of how a vapor–liquid interface affects freezing in its vicinity is therefore still a major open question in ice physics. Here, we address this question computationally by using the forward-flux sampling algorithm to compute the nucleation rate in a freestanding nanofilm of supercooled water. We use the TIP4P/ice force field, one of the best existing molecular models of water, and observe that the nucleation rate in the film increases by seven orders of magnitude with respect to bulk at the same temperature. By analyzing the nucleation pathway, we conclude that freezing in the film initiates not at the surface, but within an interior region where the formation of double-diamond cages (DDCs) is favored in comparison with the bulk. This, in turn, facilitates freezing by favoring the formation of nuclei rich in cubic ice, which, as demonstrated by us earlier, are more likely to grow and overcome the nucleation barrier. The films considered here are ultrathin because their interior regions are not truly bulk-like, due to their subtle structural differences with the bulk.

ice | nucleation | molecular simulations | surface freezing | statistical mechanics

Freezing of water into ice is ubiquitous in nature and can occur in a wide range of environments, from biological cells (1) and soil (2) to meteors (3) and atmospheric clouds (4). Ice formation is particularly important in the atmospheric processes that exert a major influence on our weather and climate. Indeed, the radiative properties (4) and precipitation propensity (5) of a cloud are both determined by the amount of ice that it harbors. Not surprisingly, the liquid fraction of clouds is an extremely important input parameter in meteorological models (6). Freezing is a first-order phase transition and proceeds through a mechanism known as nucleation and growth. In mixed-phase clouds, which are responsible for the bulk of land surface precipitation (7), freezing is usually nucleation-limited, and individual freezing events are rare. Predicting the timing of such rare freezing events is important in modeling cloud microphysics. However, nucleation rates, which are volume- or area-normalized inverse nucleation times, can only be measured experimentally over a narrow range of temperatures and pressures (8), and extrapolations to other temperatures are nontrivial (9). In nature, homogeneous nucleation of ice is only likely at very low temperatures, and the majority of freezing events in mixed-phase clouds occur heterogeneously, at interfaces provided by external insoluble entities known as ice-nucleating agents. Understanding the nature of such interfaces, and how they impact the nucleation kinetics, is very important in atmospheric sciences, and yet remains a challenging problem. Because of these difficulties, predicting the liquid fraction of a cloud is a demanding component of climate modeling and is prone to considerable uncertainties (10). Developing a comprehensive framework for predicting atmospheric ice nucleation is therefore one of the major open challenges of atmospheric sciences.

One major difficulty in constructing such predictive frameworks is the inability to determine the proper scaling of volumetric nucleation rates with the size of microdroplets and nanodroplets that constitute clouds. This is practically important because atmospheric clouds are composed of droplets of different sizes. This scaling is determined by whether freezing is enhanced or suppressed near vapor–liquid interfaces. If freezing is suppressed at a free interface, the effective volumetric nucleation rate will be independent of r, the droplet radius, and bulk freezing will be dominant at all sizes. In contrast, an enhancement of freezing at free surfaces will lead to an effective volumetric nucleation rate that decreases with r, and there will be a critical radius, r_c, below which surface freezing will become dominant. Understanding the effect of free surfaces on freezing is also important from an engineering perspective, because it can provide novel avenues for controlling atmospheric ice nucleation by manipulating vapor–liquid interfaces (e.g., through the addition of surfactants).

The question of surface freezing in materials is of theoretical and practical importance. For instance, it is known that several materials, such as normal alkanes (11), alcohols (12), and certain alloys (13), can undergo surface freezing. However, it is not yet known with predictive certainty what makes a material susceptible to surface-induced crystallization. The simplest possible criterion, which can also be obtained from classical nucleation theory, is discussed in detail by Tabazadeh and coworkers (14, 15), who argue that a liquid that partially wets its crystal is prone to freeze at a free interface. The partial wettability condition follows from the Young equation and is given by $\sigma_{ls} < \sigma_{sv} - \sigma_{lv}$, with σ_{ls}, σ_{sv} and σ_{lv}, the solid–liquid, solid–vapor, and liquid–vapor surface tensions, respectively. Despite its simplicity, it is extremely

Significance

Ice nucleation at interfaces plays an important role in atmospheric processes. Because of the insufficient spatiotemporal resolution of the existing experimental techniques, however, it is very difficult to understand how interfaces affect freezing at the molecular level. In particular, whether a vapor–liquid interface enhances or suppresses freezing at its vicinity is still a major unresolved question in contemporary ice physics. We address this question computationally by directly calculating the ice nucleation rate in a freestanding nanofilm of supercooled water modeled using an accurate molecular model and observe seven orders of magnitude enhancement. We observe that freezing initiates away from the air–water interface, in regions of the film favorable to the formation of cubic ice.

Author contributions: A.H.-A. and P.G.D. designed research; A.H.-A. performed research; A.H.-A. and P.G.D. analyzed data; and A.H.-A. and P.G.D. wrote the paper.

Reviewers: C.D., University of Vienna; and A.M., University College London.

The authors declare no conflict of interest.

[1]Present address: Department of Chemical and Environmental Engineering, Yale University, New Haven, CT 06520.

[2]To whom correspondence should be addressed. Email: pdebene@princeton.edu.

This article contains supporting information online at www.pnas.org/lookup/suppl/doi:10.1073/pnas.1620999114/-/DCSupplemental.

difficult to determine whether this criterion is satisfied for a given material due to the challenges of measuring surface tensions in the supercooled regime (16). Not surprisingly, this criterion is not quantitatively verified for water in ref. 14, and only a qualitative argument is given as to why this substance is expected to satisfy this criterion and undergo surface freezing.

Because of their insufficient spatiotemporal resolution, the existing experimental techniques have so far been incapable of directly confirming or disproving surface freezing in water. The most direct anecdotal evidence obtained so far is the observation that contact freezing (i.e., heterogeneous nucleation caused by the presence of a solid particle close to a vapor–liquid interface) occurs at rates considerably higher than immersion freezing (i.e., heterogeneous nucleation caused by the presence of a solid particle in the bulk) (17). All efforts in this regard, including the analysis carried out in ref. 14, have therefore been indirect and have focused on examining the dependence of volumetric nucleation rates on the droplet size distribution (18, 19), with the studied droplets usually between 1 and 100 μm in diameter. Such studies, however, have been inconclusive with respect to the core question of surface freezing in water due to the large uncertainties in droplet size distributions and nucleation rates and the fact that surface freezing becomes potentially dominant at droplet sizes of a few micrometers, which lies at the lower end of sizes considered in such studies (20). Probing nucleation kinetics at the nanoscale (e.g., in nanofilms and nanodroplets) poses further complications. For instance, nanodroplets typically have large Laplace pressures, and their freezing occurs at lower temperatures and culminates in the formation of stacking disordered ice, a polymorph different from hexagonal ice that is the final product of freezing in microdroplets (21, 22). This makes the proper comparison of rate measurements in nanodroplets and microdroplets nontrivial. The question of surface freezing in water is therefore still unresolved and is considered one of the 10 major open questions concerning ice and snow (23).

The lack of convincing direct experimental evidence for (or against) surface freezing in water has made molecular simulation an attractive alternative. Depending on the force fields and system sizes considered, however, such computational studies have reached conflicting conclusions. For example, molecular dynamics (MD) simulations of freestanding nanofilms simulated using a six-site force field (24) reveal that freezing occurs predominantly at the surface (25, 26), an observation attributed to the lack of electrostatic neutrality in the subsurface region. Because of the small system sizes ($N = 384$–576) considered in refs. 25 and 26, however, these findings were likely affected by considerable finite size effects. The model of choice for the overwhelming majority of computational studies of surface freezing has been the coarse-grained monoatomic water (mW) potential (27). Li et al. (28) and Haji-Akbari et al. (29) use forward-flux sampling (FFS) (30) to compute nucleation rates in droplets (28) and freestanding thin films (29) of supercooled mW. By comparing the nucleation rates in the bulk (29, 31) and in confined (28, 29) geometries, they both conclude that surface freezing is suppressed in the mW system. These findings are interesting in the sense that the mW system satisfies (32) the partial wettability condition articulated in refs. 14 and 15, and yet fails to undergo surface freezing. Another feature that correlates with surface freezing propensity in silicon, another tetrahedral liquid, is the negative slope of dP/dT, the melting curve in the phase diagram (33). Materials with negative dP/dT need to undergo expansion upon freezing, which is presumably facilitated at free interfaces. However, it has been demonstrated that the mW system (29) and some of its variants (34) fail to undergo surface freezing despite satisfying this criterion. The fact that surface freezing propensity fails to correlate with simple thermodynamic features, such as partial wettability of the crystal or the negative slope of the melting curve, underscores the complexity of the surface freezing process and the possibility that it can be affected by system-specific structural features.

Despite providing valuable insight into the underlying physics of surface freezing, the findings obtained with the mW model might not be representative of how real water behaves close to free surfaces, both due to this model's coarse-grained nature and its lack of electrostatic interactions, which can potentially play a pivotal role in interfacial phenomena. For the more realistic molecular models, however, a systematic investigation of surface freezing was not possible until recently because direct calculations of nucleation rates were out of reach. Recently, we used a coarse-grained variant of the FFS algorithm to perform the first direct calculation of the bulk homogeneous ice nucleation rate (35) in the TIP4P/ice system (36), which is one of the most accurate molecular models of water and the best model for studying ice polymorphs. This development enables us to consider the question of surface freezing in the TIP4P/ice system by computing volumetric nucleation rates in freestanding nanofilms and comparing those with the already-computed nucleation rates in the bulk. The rationale for preferring nanofilms over nanodroplets is the net zero curvature of free interfaces in nanofilms. This allows us to explore exclusively the effect of a free interface on the kinetics and mechanism of nucleation. For nanodroplets, however, changes in nucleation kinetics will be due to the combined effect of the free interface and the large Laplace pressures that it induces inside the droplet, and disentangling the two is nontrivial. Furthermore, the curvature at free interfaces in atmospheric microdroplets is orders of magnitude smaller than in the case of nanodroplets. Accordingly, the former are accurately represented by zero-curvature freestanding nanofilms.

Results and Discussion

Rate Calculations. We compute nucleation rates using the coarse-grained FFS algorithm that we introduced and discussed in detail in an earlier publication (35). In every FFS calculation, it is necessary to first define an order parameter, $\lambda(\mathbf{x}^N)$, that quantifies the progress of the kinetic process of interest—nucleation in our case—with the liquid, L, and crystalline, X, basins characterized by $\lambda(\mathbf{x}^N) \leq \lambda_L$ and $\lambda(\mathbf{x}^N) \geq \lambda_X$, respectively, and $\mathbf{x}^N$ denoting the N-body system's configuration. The nucleation rate is then given by the cumulative flux of trajectories that leave λ_L and end up in λ_X, and is estimated as the cumulative product of Φ_0, the flux of trajectories that leave λ_L and cross $\lambda(\mathbf{x}^N) = \lambda_1 > \lambda_L$ and p_k values, the transition probabilities of going from λ_k to λ_{k+1}. Here, $\lambda_L < \lambda_1 < \lambda_2 < \cdots < \lambda_n = \lambda_X$ are milestones that lie between the two basins. We compute the nucleation rate in a 4-nm-thick freestanding film of supercooled water with 3,072 TIP4P/ice molecules. To be consistent with our earlier rate calculation in the bulk, performed at 230 K and 1 bar (35), we conducted this new calculation at 230 K. We also used the same order parameter (i.e., the size of the largest crystallite in the system).

Fig. 1 depicts the cumulative growth probability $\mathbb{P}(\lambda_k|\lambda_1) = \prod_{j=1}^{k-1} p_j$ as a function of λ for both the bulk and confined geometries. It can be seen, in the first place, that the volumetric ice

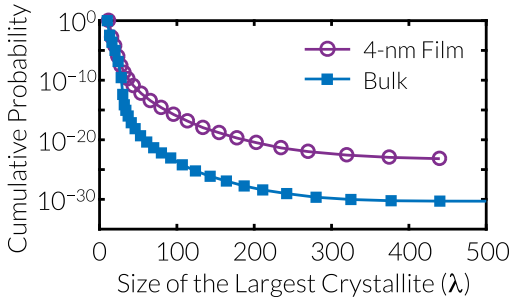

Fig. 1. Cumulative transition probabilities vs. the size of the largest crystallite in the system for the bulk and film geometries at 230 K. The volumetric nucleation rates are $\log_{10}J[\mathrm{m}^{-3}\cdot\mathrm{s}^{-1}] = 12.5819 \pm 0.4961$ and 5.9299 ± 0.5863 for the film and bulk geometries, respectively.

nucleation is almost seven orders of magnitude larger in the film geometry. This is contrary to what we had previously observed in the coarse-grained mW system, in which the nucleation rate decreases by seven orders of magnitude in going from the bulk to a 2.5-nm-thick freestanding nanofilm (29). This marked qualitative difference between the two systems is remarkable and will be further discussed below.

Nucleation Mechanism. Another distinction between the bulk and confined cases is the lack of a pronounced inflection in the cumulative probability curve for the film (Fig. 1). As discussed in ref. 35, the pronounced inflection in the bulk is due to the competition between double-diamond cages (DDCs) (Fig. 2*A*) and hexagonal cages (HCs) (Fig. 2*B*) that are the topological building blocks of cubic and hexagonal polymorphs of ice, respectively. Unlike DDCs, which are symmetric, and therefore support uniform accretion of new cages, HCs are asymmetric, and tend to grow faster along their prismatic (side) faces in comparison with their basal (top/bottom) faces. This asymmetric growth leads to the formation of chains of prismatically connected HCs in HC-rich crystallites and puts them at a disadvantage during early stages of nucleation. The inflection in Fig. 1 is therefore caused by the initial explosion of prismatically growing HC-rich nuclei, followed by their subsequent extinction due to their higher asphericity. This makes the surviving configurations (i.e., the configurations that have progeny beyond the inflection region) significantly more DDC-rich—and less HC-rich—as depicted in Fig. 2 *C* and *D*. The same is true in the film geometry because the surviving configurations are still more DDC-rich, and correspondingly less HC-rich, than the vanishing configurations that do not contribute to the nucleation pathway (Fig. 2 *E* and *F*). The absolute HC participation, however, is significantly lower in the film geometry. This suppresses the potential adverse effect of HCs on the growth of crystallites and leads to the virtual disappearance of the inflection region otherwise observed in the bulk.

To understand the origin of these marked differences between bulk and confined geometries, we inspect the spatial distribution of largest crystallites within the film at different values of λ. To make sense of such distributions, however, we first need to identify the regions of the film that are directly affected by free interfaces. It is well established that confinement breaks the translational isotropy of the stress tensor $S(z)$, making its normal, $S_{zz}(z)$ and lateral, $S_{xx}(z) = S_{yy}(z)$, components nonidentical. Here, z is the distance from the center of the film. The anisotropy in $S(z)$ can thus be used, to a first approximation, as a criterion for identifying the subsurface region (37). Toward that goal, we

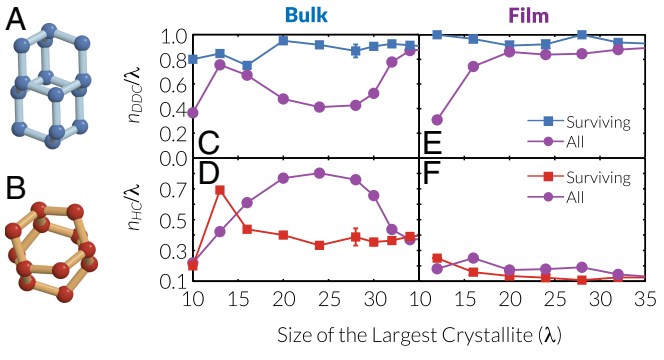

Fig. 2. (*A* and *B*) Cage types: DDCs (*A*) and HCs (*B*) are the topological building blocks of cubic and hexagonal ice, respectively. (*C*–*F*) Cage participation of the molecules that are part of the largest crystallite in DDCs (*C* and *E*) and HCs (*D* and *F*) in bulk (*C* and *D*) and film (*E* and *F*) geometries. The surviving configurations are the configurations that have progeny at $\lambda = 41$ and 66 for bulk and film geometries, respectively. The two fractions do not add up to unity because a molecule can be both part of a DDC and an HC. The first three "surviving" data points in *C* and *D* and the first surviving data point in *E* and *F* correspond to a single configuration each, and thus have no error bars.

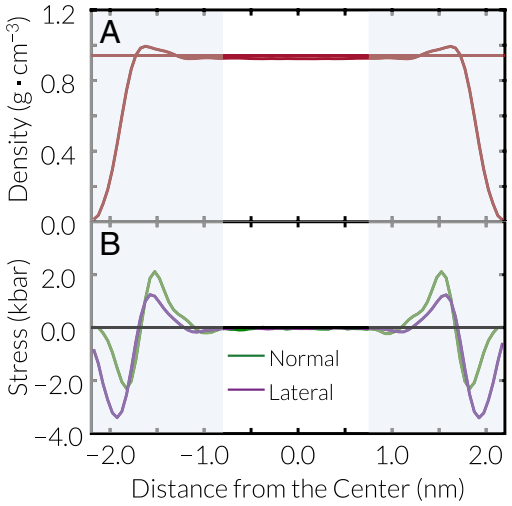

Fig. 3. Spatial distribution of density (*A*) and normal and lateral stress (*B*) in a 4-nm-thick freestanding film of the TIP4P/ice system at 230 K simulated for 5 μs. The shaded blue regions correspond to the subsurface regions as determined from anisotropy in the normal and lateral components of the stress tensor.

carry out regular MD simulations of 4-nm-thick TIP4P/ice films and compute density and stress using the approach outlined in ref. 38. Using the stress tensor anisotropy as a criterion, the subsurface region is determined to be ~1.5 nm thick (Fig. 3). Like stress, density converges to its bulk value, albeit over slightly shorter length scales.

Upon identifying the subsurface region, we inspect the spatial spread of the largest crystallites obtained from FFS by constructing a histogram of the z coordinates of water molecules that belong to such crystallites. Considering the enhancement of freezing in the film (with respect to the bulk), it is intuitively expected that the histogram would be peaked in the subsurface region. Strikingly, the opposite behavior is observed and the largest crystallites emerge not in the shaded blue regions, but in the interior of the film that presumably exhibits bulk-like thermodynamic behavior (Fig. 4). Despite the fact that for $\lambda_1 = 12$, the largest crystallites are equally distributed across the film (Fig. 4*B*), the surviving configurations (i.e., the ones with progeny at $\lambda = 66$) are always exclusively located in the interior region (Fig. 4*A*). This suggests that the interior region is not truly bulk-like (otherwise, Fig. 4 would suggest that the overall rate should be similar to that calculated for the bulk, up to a trivial geometric factor to account for the fraction of the film geometry that is "active"), and there exists a structural observable that decays to its bulk value over a characteristic length scale, l_c, which is significantly larger than l_s, the thickness of the subsurface region.

Considering the importance of the interplay between HCs and DDCs in the nucleation process, and the stark difference between the HC and DDC content of the largest crystallites in bulk and film geometries, we compute $\rho_{HC}(z)$ and $\rho_{DDC}(z)$, the HC and DDC number densities, across the film and compare those with their respective bulk values. As for the bulk, we determine HC and DDC densities from NpT MD simulations at 230 K and 1 bar and obtain $\rho_{HC,bulk} = 0.0602(7)$ nm^{-3} and $\rho_{DDC,bulk} = 0.0319(8)$ nm^{-3}, respectively. For the film geometry, we compute $\rho_{HC}(z)$ and $\rho_{DDC}(z)$ profiles by analyzing the MD trajectories used for computing the profiles shown in Fig. 3. We also compute the spatial profile of local q_6, an orientational bond order parameter (39) that quantifies the local extent of ice-like order around each molecule. As demonstrated in Fig. 5*B*, in the shaded blue subsurface region, both $\rho_{HC}(z)$ and $\rho_{DDC}(z)$ are significantly lower than their respective bulk values. However, DDCs are more strongly depleted, with $\psi(z) := \rho_{HC}(z)/\rho_{DDC}(z)$, the HC/DDC ratio, significantly exceeding its bulk value of

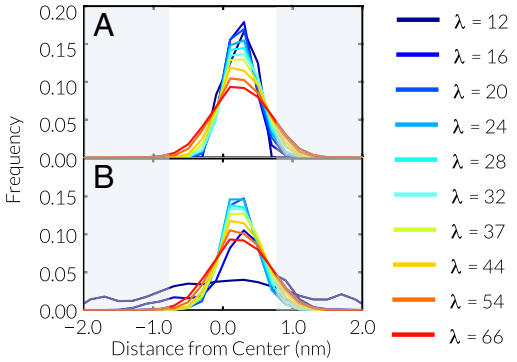

Fig. 4. Spatial distribution of molecules that belong to the largest crystallites for different values of λ for surviving configurations that have progeny at $\lambda = 66$ (*A*) and all configurations at a given λ (*B*). The shaded blue regions correspond to the subsurface regions determined from anisotropy of the stress tensor.

$\psi_{\text{bulk}} = 1.88(5)$ (Fig. 5*C*). The paucity of both cage types and the stronger depletion of DDCs make the subsurface region an unfavorable environment for the formation of nascent small crystallites. This explains why nucleation does not start at the subsurface region.

Unlike the subsurface region, $\psi(z)$ is significantly lower than ψ_{bulk} in the interior region, which thus provides a more favorable environment for the formation of DDCs. This, in turn, facilitates nucleation and leads to elevated rates by suppressing the HC-induced inflection observed in the bulk. Consistent with this hypothesis, the majority of water molecules belonging to the largest crystallites reside in this low-ψ region (Fig. 4). Interestingly, such deviations persist even in films as thick as 9 nm (Fig. S1 *C* and *D*), pointing to l_c values that are much larger than $l_s \sim 1.5$ nm. We observe a similar lack of convergence to the bulk in $q_6(z)$ profiles that are always larger than and never converge to $\langle q_6 \rangle_{\text{bulk}} = 0.254$ in the interior region (Fig. 5*A* and Fig. S1*B*). Higher q_6 values in the interior region are indeed consistent with higher cubicity because the value corresponding to cubic ice, $\langle q_6 \rangle_{\text{cubic}} = 0.800$ is larger than the corresponding hexagonal value, $\langle q_6 \rangle_{\text{hex}} = 0.690$ (31, 35).

Surface Freezing in the mW System. Unlike in TIP4P/ice, surface freezing is suppressed in the coarse-grained mW system (28, 29). To explore the origin of this different behavior, we perform the same type of cage statistics analysis in the mW system, at the same temperature (and pressure) as TIP4P/ice. Note that this corresponds to the same degree of supercooling because both models have realistic melting temperatures (27, 36). In the bulk, at 230 K and 1 bar, the HC and DDC number densities and the HD-to-DDC ratio are given by $\rho^{\text{mW}}_{\text{HC,bulk}} = 0.02099(3)$ nm^{-3}, $\rho^{\text{mW}}_{\text{DDC,bulk}} = 0.00465(2)$ nm^{-3} and $\psi^{\text{mW}}_{\text{bulk}} = 4.51(2)$, respectively. (See *SI Text* for a comparison of bulk cage statistics in the TIP4P/ice and mW systems.) We also compute the spatial profiles of density, stress, $\rho_{\text{HC}}(z)$, $\rho_{\text{DDC}}(z)$, and $\psi(z)$ for a 20-nm-thick mW film at 230 K (Fig. 6). The subsurface regions, as determined from the anisotropy of the stress tensor, have similar thicknesses in the TIP4P/ice and mW films (Fig. 6*A*). Furthermore, they both have fewer cages (Fig. 6*B*) and larger $\psi(z)$ values (Fig. 6*C*) than the bulk. Beyond the subsurface region, however, $\psi(z)$ is almost never smaller than $\psi^{\text{mW}}_{\text{bulk}}$. This is in sharp contrast to TIP4P/ice films that have extended interior regions with lower-than-bulk $\psi(z)$ values. Similarly, $q_6(z)$ behaves like the other thermodynamic properties in the mW system and is never higher than $\langle q_6 \rangle^{\text{mW}}_{\text{bulk}} = 0.251$ in the interior region (Fig. S2). In other words, confinement does not lead to the formation of low-ψ regions in mW films, and all it does is to amplify ψ in the subsurface region. It is therefore no surprise that surface freezing is suppressed in the mW system.

Similar to TIP4P/ice, the decay length scale for the deviations of cage density profiles and $\psi(z)$ from the bulk is significantly larger than the thickness of subsurface region in the mW system (Fig. S3), even though the magnitude of such deviations are considerably smaller. It might therefore be interesting to explore the possible generality of the inequality, $l_c \gg l_s$. The stark difference between decay characteristics of simple thermodynamic properties, such as stress, and complex structural features, such as cage density, underscores the difficulty of identifying regions with bulk-like behavior in confined systems, especially when it comes to phenomena as complex as nucleation. Determining what constitutes "ultrathin" is therefore a subtle question and requires careful examination of all thermodynamic and structural properties that could be relevant to the phenomenon under consideration.

The development of the coarse-grained mW potential has been a major breakthrough in computational studies of water and has considerably expanded the range of accessible time and length scales (40). The popularity of mW is not only a consequence of its efficiency, but also of its remarkable success in reproducing thermodynamic and structural features of water (27). This work suggests that this very successful model might not be able to accurately capture subtle interfacial phenomena of the type reported in this work. The mW model has also been shown to differ qualitatively from atomistic models in other aspects, such as the presence of a liquid–liquid critical point (41).

Comparison with Earlier Experimental Work. As outlined above, directly addressing the surface freezing problem in experiments is extremely challenging. Comparing our computed rate with rate measurements in ultraconfined geometries such as nanodroplets (21, 22) is not straightforward, because the latter are typically done at lower temperatures and higher (Laplace) pressures. Extrapolating those rates to 230 K and 1 bar not only involves predicting the thermodynamic and transport properties of supercooled water at experimentally inaccessible conditions

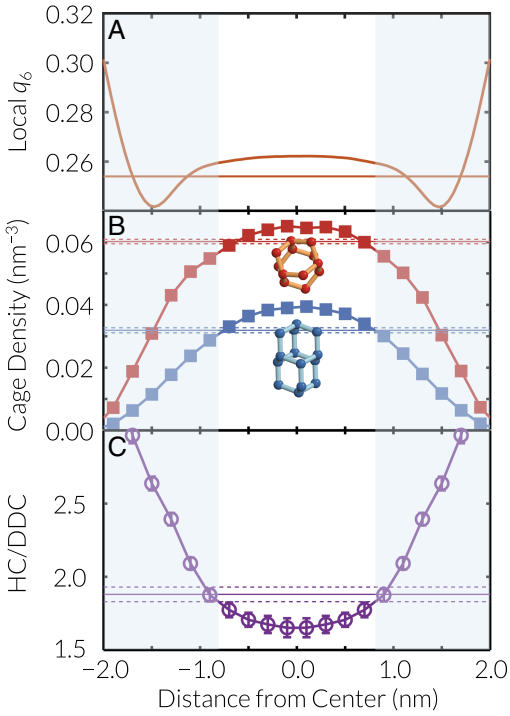

Fig. 5. Spatial distributions of local q_6 (*A*), cage number densities (*B*), and HC/DDC ratio (*C*) across the 4-nm-thick TIP4P/ice film. The subsurface region, as determined from the anisotropy in the stress tensor, is shaded in blue. Bulk values and the corresponding error bars are depicted with straight lines and dashed lines, respectively. In *B*, the symbols are larger than the error bars.

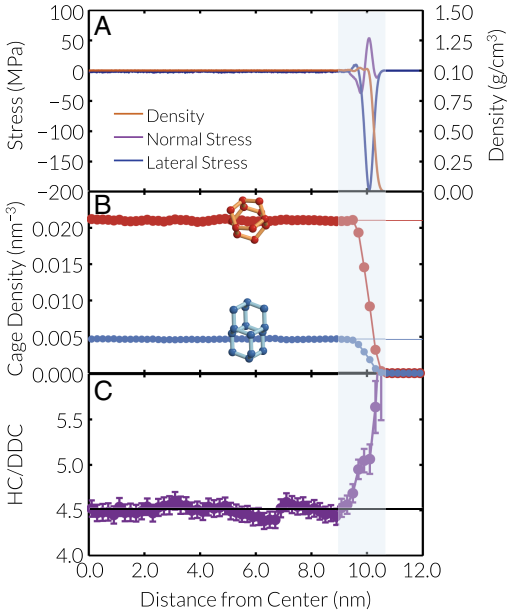

Fig. 6. Spatial profiles of density and normal and lateral stress (*A*), $\rho_{HC}(z)$ and $\rho_{DDC}(z)$ (*B*), and $\psi(z)$ (*C*) as a function of distance from the center of a 20-nm-thick film of mW water at 230 K. The shaded blue region corresponds to the subsurface region as determined per anisotropy of the stress tensor.

(high pressures, low temperatures), but also requires making certain quantitative assumptions about the importance of surface freezing (9), the very question that we attempt to address in this work. On the simulation side, every computational study of nucleation is limited by the accuracy of the used force field. As discussed elsewhere (28, 31, 35, 42–44), even modest differences between experimental and simulation values of the thermodynamic driving force, $|\Delta\mu|$ (i.e., the free energy difference between the supercooled liquid and the stable crystal), and the solid–liquid surface tension, γ_{ls}, can result in considerable errors in the estimation of nucleation rates.

Considering these limitations, we use observables other than the actual rates in our comparison with experiments. One such observable is the extent by which the effective volumetric nucleation rate changes upon confinement. Recently, Laksmono et al. (9) used femtosecond X-ray imaging to estimate that the maximum bulk nucleation rate in water's deeply supercooled region is $\log_{10} J_{max}[m^{-3} \cdot s^{-1}] = 20.5 \pm 1.5$, which is 7–10 orders of magnitude smaller than effective volumetric nucleation rates in nanodroplets (21, 22). Although this observation might be explained by invoking a fragile-to-strong transition in liquid water (3, 9), it is also not inconsistent with the direction of the present predictions (i.e., the possibility of surface-enhanced freezing). Interestingly, our predicted confinement-induced enhancement of the effective volumetric nucleation rate is also consistent with the 7–10 orders of magnitude gap predicted in ref. 9. Similarly, it has been observed in a separate study that heterogeneous nucleation at a free interface is 10 orders of magnitude faster than in the bulk (17), an enhancement also very close to our predicted 7-orders-of-magnitude surface-induced enhancement of the homogeneous nucleation rate.

Another important observable is r_c, the critical droplet radius below which surface freezing becomes dominant. In principle, an atmospheric droplet could either undergo bulk nucleation, with a volumetric nucleation rate J, or surface nucleation, with an aereal nucleation rate J_a. Assuming that J_a does not depend on curvature, r_c will be given by $r_c = 3J_a/J$. Considering the technical difficulties outlined in the introduction, r_c has not been determined experimentally, but is not expected to exceed a few micrometers (20). In a freestanding film of thickness d with an effective volumetric nucleation rate J_v, J_a is given by $J_a = J_v d/2$. This gives us an estimate of $\log_{10} J_a[m^{-2} \cdot s^{-1}] = 3.8829 \pm 0.4961$. Using the nucleation rate reported in ref. 35, we obtain $\log_{10} r_c[m] = -1.5699 \pm 0.7680$, which is roughly four orders of magnitude larger than the expected $r_c \sim O(10^{-6}m)$. The thin films that we have studied (4 nm in Fig. 5; 9 nm in Fig. S1) lack a properly developed bulk region, in that $q_6(z)$ and $\psi(z)$ never reach their bulk values (contrast with Fig. 6*C* and Fig. S2 for mW). Hence, within the range of film thicknesses that we find to be computationally tractable, although the presence of free surfaces profoundly influences both rate and mechanism of ice nucleation, we do not see a clear separation between surface and bulk nucleation. Such a separation would be needed to properly compute r_c.

Our calculations, in other words, suggest the existence of at least three regimes: ultrathin, thin, and thick films. In the first, which we study here, the subsurface regions are connected by a region that has some bulk characteristics (density and stress isotropy), but lacks others (q_6 and cage distribution). Thin films would be thin enough for surface nucleation to be dominant, and yet thick enough to possess a well-developed bulk region. Finally, thick films would be dominated by bulk nucleation and would possess a well-developed bulk region.

Comparison with Other Molecular Models. As mentioned in the introduction, earlier computational studies of freestanding nanofilms using a six-site molecular water model also reveal the enhancement of freezing at free interfaces (25, 26). Despite reaching the same conclusion as this work, the mechanism of enhancement in refs. 25 and 26 is different, with the authors observing that most freezing events initiate in the immediate vicinity of the interface. They attribute this to the lack of electrostatic neutrality at the free interface, where water molecules tend to favor orientations in which the hydrogen atoms face the vapor phase. Even though a similar lack of electrostatic neutrality in the subsurface is observed in TIP4P/ice films (Fig. S4), freezing tends to start at the electrically neutral deeper regions of the film (Fig. 4*A*). In other words, orientational ordering of water molecules at the interface does not tend to facilitate nucleation for the subtle structural reasons discussed in the text. This underscores the importance of caution in interpreting the effect of interfacial ordering on nucleation kinetics, because "bad" ordering can suppress—rather than facilitate—nucleation. This latter point has been recently demonstrated in other computational studies of ice nucleation as well (45).

Conclusions

In this work, we investigate the longstanding question of surface freezing in water. We use the FFS technique to directly compute the rate of ice nucleation in freestanding water nanofilms, simulated using the TIP4P/ice force field, which is one of the best molecular models of water. We observe that nucleation is enhanced by seven orders of magnitude in the film geometry, and is yet "homogeneous" in nature, with the crystallites emerging not in the subsurface region, but within the interior of the film. We attribute this counterintuitive behavior to the more favorable environment that emerges for the formation of DDCs within the interior region. As demonstrated earlier, DDCs play a constructive role in the nucleation process due to their rather uniform growth, and their preferential emergence in the interior region makes the nucleation process easier to proceed. Our findings suggest that surface freezing might be driven by structural features that decay over much larger length scales than simple thermodynamic properties. The films considered in this work are ultrathin in the sense that they have interior regions that possess some but not all bulk characteristics. The computational survey of all regimes (ultrathin, thin, and thick) still remains a major open challenge.

Methods

All MD simulations are performed by using large-scale atomic/molecular massively parallel simulator (LAMMPS) (46) using the velocity Verlet

algorithm with a time steps of 2 and 10 fs for the TIP4P/ice and mW systems, respectively (47). In the TIP4P/ice system, rigidity constraints are maintained by using SHAKE (48), and long-range electrostatic interactions are computed by using the particle–particle particle–mesh algorithm (49) with a short-range cutoff of 0.85 nm. Bulk and film simulations are carried out in the *NpT* and *NVT* ensembles, respectively, with temperature and pressure controlled by using the Nosé–Hoover thermostat (50, 51) and the Parrinello–Rahman barostat (52), respectively. Nucleation rates are computed using the coarse-grained variant of the FFS algorithm described in ref. 35 with a sampling time of $\tau_s = 1$ ps. The order parameter is chosen as the number of water molecules in the largest crystallite, determined using the Steinhardt q_6 order parameter (39) and the chain exclusion algorithm of Reinhardt (53). The FFS calculation amounts to a total of 376 μs of MD trajectories, which is equivalent to 7.5 million CPU-hours on the Stampede supercomputer. Further details of FFS are given in *SI Text*. HCs and DDCs are detected by using the topological criteria outlined in ref. 35. For both q_6 calculations and ring identification, a distance cutoff of 0.32 nm between oxygen atoms is used.

Spatial profiles of thermodynamic quantities are determined from conventional isochoric, isothermal (NVT) MD simulations, using a simple binning approach (38) with a bin thickness of 0.05 nm. The q_6 spatial profile is defined as $q_6(z) := \langle \sum_{i=1}^{N} q_{6,i}\delta(z_i - z)\rangle / \sum_{i=1}^{N} \delta(z_i - z)\rangle$, with N and $q_{6,i}$ the number of water molecules, and the local q_6 of molecule i, respectively. For $\rho_{HC}(z)$ and $\rho_{DDC}(z)$ calculations, thicker 0.2-nm bins are used, and each cage's contribution is equally distributed among the bins that it intersects (see *SI Text* for details). For all film calculations, initial configurations are prepared by melting a slab of cubic ice at $T = 350$ K, saving independent configurations separated by a minimum of 0.4 ns, and gradually quenching each configuration to the final temperature of 230 K. Cage statistics in the bulk are computed in *NpT* MD simulations at 230 K and 1 bar, with the starting configurations prepared using the procedure described in refs. 29 and 35. Further details of the conducted MD simulations are given in Table S2.

ACKNOWLEDGMENTS. We thank I. Cosden for his assistance in securing computational resources for this calculation. P.G.D. was supported by National Oceanic and Atmospheric Administration Cooperative Institute for Climate Science Award AWD 1004131; and the Princeton Center for Complex Materials, a Materials Research Science and Engineering Center (MRSEC) supported by National Science Foundation (NSF) Grant DMR-1420541. These calculations were performed on the Terascale Infrastructure for Groundbreaking Research in Engineering and Science at Princeton University and the Yale Center for Research Computing. This work also used the Extreme Science and Engineering Discovery Environment, which is supported by NSF Grant ACI-1053575.

1. Haji-Akbari A (2016) Rating antifreeze proteins: Not a breeze. *Proc Natl Acad Sci USA* 113:3714–3716.
2. Chamberlain EJ, Gow AJ (1979) Effect of freezing and thawing on the permeability and structure of soils. *Eng Geol* 13:73–92.
3. Jenniskens P, Blake DF (1996) Crystallization of amorphous water ice in the solar system. *Astrophys J* 473:1104–1113.
4. Baker MB (1997) Cloud microphysics and climate. *Science* 276:1072–1078.
5. Carslaw KS, Harrison RG, Kirkby J (2002) Cosmic rays, clouds, and climate. *Science* 298:1732–1737.
6. Fowler LD, Randall DA, Rutledge SA (1996) Liquid and ice cloud microphysics in the CSU general circulation model. Part 1: Model description and simulated microphysical processes. *J Clim* 9:489–529.
7. Mülmenstädt J, Sourdeval O, Delanoë J, Quaas J (2015) Frequency of occurrence of rain from liquid-, mixed-, and ice-phase clouds derived from a-train satellite retrievals. *Geophys Res Lett* 42:6502–6509.
8. Kohl I, Bachmann L, Hallbrucker A, Mayer E, Loerting T (2005) Liquid-like relaxation in hyperquenched water at $\leq$140 K. *Phys Chem Chem Phys* 7:3210–3220.
9. Laksmono H, et al. (2015) Anomalous behavior of the homogeneous ice nucleation rate in "no-man's land". *J Phys Chem Lett* 6:2826–2832.
10. Herbert RJ, Murray BJ, Dobbie SJ, Koop T (2015) Sensitivity of liquid clouds to homogenous freezing parameterizations. *Geophys Res Lett* 42:1599–1605.
11. Ocko BM, et al. (1997) Surface freezing in chain molecules: Normal alkanes. *Phys Rev E* 55:3164–3182.
12. Gang O, Wu X, Ocko B, Sirota E, Deutsch M (1998) Surface freezing in chain molecules. II. Neat and hydrated alcohols. *Phys Rev E* 58:6086–6100.
13. Shpyrko OG, et al. (2006) Surface crystallization in a liquid AuSi alloy. *Science* 313: 77–80.
14. Tabazadeh A, Djikaev YS, Reiss H (2002) Surface crystallization of supercooled water in clouds. *Proc Natl Acad Sci USA* 99:15873–15878.
15. Djikaev Y, Tabazadeh A, Hamill P, Reiss H (2002) Thermodynamic conditions for the surface-stimulated crystallization of atmospheric droplets. *J Phys Chem A* 106(43):10247–10253.
16. Gránásy L, Pusztai T, James PF (2002) Interfacial properties deduced from nucleation experiments: A Cahn–Hilliard analysis. *J Chem Phys* 117:6157.
17. Shaw RA, Durant AJ, Mi Y (2005) Heterogeneous surface crystallization observed in undercooled water. *J Phys Chem B* 109:9865–9868.
18. Duft D, Leisner T (2004) Laboratory evidence for volume-dominated nucleation of ice in supercooled water microdroplets. *Atmos Chem Phys Discuss* 4:3077–3088.
19. Kuhn T, Earle ME, Khalizov AF, Sloan JJ (2011) Size dependence of volume and surface nucleation rates for homogeneous freezing of supercooled water droplets. *Atmos Chem Phys* 11:2853–2861.
20. Sigurbjörnsson OF, Signorell R (2008) Volume versus surface nucleation in freezing aerosols. *Phys Rev E* 77:051601.
21. Huang J, Bartell LS (1995) Kinetics of homogeneous nucleation in the freezing of large water clusters. *J Phys Chem* 99:3924–3931.
22. Bhabhe A, Pathak H, Wyslouzil BE (2013) Freezing of heavy water (D_2O) nanodroplets. *J Phys Chem A* 117:5472–5482.
23. Bartels-Rausch T (2013) Chemistry: Ten things we need to know about ice and snow. *Nature* 494:27–29.
24. Nada H, van der Eerden JPJM (2003) An intermolecular potential model for the simulation of ice and water near the melting point: A six-site model of H_2O. *J Chem Phys*118:7401–7413.
25. Vrbka L, Jungwirth P (2006) Homogeneous freezing of water starts in the subsurface. *J Phys Chem B* 110:18126–18129.
26. Pluhařová E, Vrbka L, Jungwirth P (2010) Effect of surface pollution on homogeneous ice nucleation: A molecular dynamics study. *J Phys Chem C* 114:7831–7838.
27. Molinero V, Moore EB (2009) Water modeled as an intermediate element between carbon and silicon. *J Phys Chem B* 113:4008–4016.
28. Li T, Donadio D, Galli G (2013) Ice nucleation at the nanoscale probes no man's land of water. *Nat Commun* 4:1887.
29. Haji-Akbari A, DeFever RS, Sarupria S, Debenedetti PG (2014) Suppression of subsurface freezing in free-standing thin films of monoatomic water. *Phys Chem Chem Phys* 16:25916–25927.
30. Allen RJ, Frenkel D, ten Wolde PR (2006) Forward flux sampling-type schemes for simulating rare events: Efficiency analysis. *J Chem Phys* 124:194111.
31. Li T, Donadio D, Russo G, Galli G (2011) Homogeneous ice nucleation from supercooled water. *Phys Chem Chem Phys* 13:19807–19813.
32. Hudait A, Molinero V (2014) Ice crystallization in ultrafine water—salt aerosols: Nucleation, ice-solution equilibrium, and internal structure. *J Am Chem Soc* 136:8081–8093.
33. Li T, Donadio D, Ghiringhelli LM, Galli G (2009) Surface-induced crystallization in supercooled tetrahedral liquids. *Nat Mater* 8:726–730.
34. Gianetti MM, Haji-Akbari A, Longinotti MP, Debenedetti PG (2016) Computational investigation of structure, dynamics and nucleation kinetics of a family of modified Stillinger–Weber model fluids in bulk and free-standing thin films. *Phys Chem Chem Phys* 18(5):4102–4111.
35. Haji-Akbari A, Debenedetti PG (2015) Direct calculation of ice homogeneous nucleation rate for a molecular model of water. *Proc Natl Acad Sci USA* 112:10582–10588.
36. Abascal JLF, Sanz E, Fernández RG, Vega C (2005) A potential model for the study of ices and amorphous water: TIP4P/Ice. *J Chem Phys* 122:234511.
37. Haji-Akbari A, Debenedetti PG (2015) Thermodynamic and kinetic anisotropies in octane thin films. *J Chem Phys* 143:214501.
38. Haji-Akbari A, Debenedetti PG (2014) The effect of substrate on thermodynamic and kinetic anisotropies in atomic thin film. *J Chem Phys* 141:024506.
39. Steinhardt PJ, Nelson DR, Ronchetti M (1983) Bond-orientational order in liquids and glasses. *Phys Rev B* 28:784–805.
40. Sosso GC, et al. (2016) Crystal nucleation in liquids: Open questions and future challenges in molecular dynamics simulations. *Chem Rev* 116:7078–7116.
41. Palmer JC, et al. (2014) Metastable liquid–liquid transition in a molecular model of water. *Nature* 510:385–388.
42. Sanz E, et al. (2013) Homogeneous ice nucleation at moderate supercooling from molecular simulation. *J Am Chem Soc* 135:15008–15017.
43. Espinosa JR, Sanz E, Valeriani C, Vega C (2014) Homogeneous ice nucleation evaluated for several water models. *J Chem Phys* 141:18C529.
44. Sosso GC, Li T, Donadio D, Tribello GA, Michaelides A (2016) Microscopic mechanism and kinetics of ice formation at complex interfaces: Zooming in on kaolinite. *J Phys Chem Lett* 7(13):2350–2355.
45. Bi Y, Cabriolu R, Li T (2016) Heterogeneous ice nucleation controlled by the coupling of surface crystallinity and surface hydrophilicity. *J Phys Chem C* 120(3):1507–1514.
46. Plimpton SJ (1995) Fast parallel algorithms for short-range molecular dynamics. *J Comput Phys* 117:1–19.
47. Swope WC, Andersen HC, Berens PH, Wilson KR (1982) A computer simulation method for the calculation of equilibrium constants for the formation of physical clusters of molecules: Application to small water clusters. *J Chem Phys* 76:637–649.
48. Ryckaert J, Ciccotti G, Berendsen H (1977) Numerical integration of the cartesian equations of motion of a system with constraints: Molecular dynamics of *n*-alkanes. *J Comp Phys* 23:327–341.
49. Hockney RW, Eastwood JW (1989) Computer Simulation Using Particles (CRC, New York).
50. Nosé S (1984) A molecular dynamics method for simulations in the canonical ensemble. *Mol Phys* 52:255–268.
51. Hoover WG (1985) Canonical dynamics: Equilibrium phase-space distributions. *Phys Rev A* 31:1695–1697.
52. Parrinello M, Rahman A (1981) Polymorphic transitions in single crystals: A new molecular dynamics method. *J Appl Phys* 52:7182–7190.
53. Reinhardt A, Doye JPK, Noya EG, Vega C (2012) Local order parameters for use in driving homogeneous ice nucleation with all-atom models of water. *J Chem Phys* 137:194504.

Supporting Information

Haji-Akbari and Debenedetti 10.1073/pnas.1620999114

SI Text

Comparison of Bulk Cage Statistics in the TIP4P/Ice and mW Systems

It is interesting to note that both cage types are less numerous in the mW system, with TIP4P/ice HC and DDC densities being three and seven times larger than their respective mW values ($\rho_{\mathrm{HC,bulk}}^{\mathrm{mW}} = 0.02099(3)$ nm^{-3} vs. $\rho_{\mathrm{HC,bulk}}^{\mathrm{TIP4P/Ice}} = 0.0602(7)$ nm^{-3}, and $\rho_{\mathrm{DDC,bulk}}^{\mathrm{mW}} = 0.00465(2)$ nm^{-3} vs. $\rho_{\mathrm{DDC,bulk}}^{\mathrm{TIP4P/Ice}} = 0.0319(8)$ nm^{-3}). ψ is therefore larger in the mW system, roughly by a factor of three. These numbers are surprising, considering the relative ease of freezing in the mW system, because one would expect fewer cages and larger ψ values to make crystallization harder. However, comparing the cage densities and ψ values of two water models that also have different thermodynamic and transport properties cannot give us predictive certainty on their ease of crystallization. Such comparisons are only relevant when conducted for the same water model under different conditions (e.g., bulk and confined geometries). As for correlations between small ψ values and ease of crystallization, it must be remembered that the detrimental impact of HCs on nucleation is primarily due to their tendency to establish prismatic connections with neighboring HCs. Therefore, a larger ψ can, in principle, be offset by lower likelihood of prismatic HC–HC connections (i.e., a lower prismatic to basal ratio, ζ). Indeed, $\zeta_{\mathrm{bulk}}^{\mathrm{mW}} = 0.99(3)$ is significantly smaller than $\zeta_{\mathrm{bulk}}^{\mathrm{TIP4P/Ice}} = 1.6(2)$, because neighboring HCs are less likely to establish prismatic connections in the mW system. As to the extent by which the ease of crystallization of a tetrahedral liquid is determined by its ψ and ζ is beyond the scope of this work and can be the subject of future studies.

Do the interior regions of TIP4P/ice and mW nanofilms have $\zeta(z)$ values that are significantly different from the bulk? This is a question that is difficult to answer, mostly due to the scarcity of HC–HC connections in the liquid that makes accurate determination of $\zeta(z)$ a challenging task. However, we analyze the MD trajectories that we use for computing profiles of thermodynamic and structural properties and conclude that $\zeta(z)$ does not exhibit any statistically significant deviation from ζ_{bulk} in TIP4P/ice (Fig. S5*A*) and mW (Fig. S5*B*). This makes our ψ-based explanation of surface freezing robust, as bulk and film geometries are identical in terms of both the used force field and the prismatic-to-basal ratio.

Definition of Cage Density Profiles

Let $\mathfrak{C}_i = \{\mathbf{r}_{i,1}, \mathbf{r}_{i,2}, \cdots, \mathbf{r}_{i,N}\}$ be the ith cage of type X ($X = $ HC, DDC) in the system, with $\mathbf{r}_{i,j} \equiv (x_{i,j}, y_{i,j}, z_{i,j})$ the position of the oxygen atom of jth water molecule in $\mathfrak{C}_i$. Let $z_{i,\min} := \min_{1\leq j\leq N} z_{i,j}$ and $z_{i,\max} := \max_{1\leq j\leq N} z_{i,j}$. Then the cage number density $\rho_X(z)$ is given by:

$$\rho_X(z) := \frac{1}{A}\left\langle \sum_{i=1}^{n} \frac{H(z - z_{i,\min})H(z_{i,\max} - z)}{z_{i,\max} - z_{i,\min}} \right\rangle \quad \textbf{[S1]}$$

Here, n is the total number of cages of type X in a given configuration, A is the surface area of the box perpendicular to the z axis, and $H(z) = \int_{-\infty}^{z} \delta(u)du$ is the Heaviside step function. Profiles of $n_b(z)$ and $n_p(z)$, the number density of basal and prismatic HC–HC connections are also computed in a similar fashion (i.e., by enumerating the z spread of water molecules that participate in each HC–HC connection).

Technical Details of FFS

The basin and first milestone are chosen as $\lambda_L = 5$ and $\lambda_1 = 12$, respectively. To determine the initial flux, Φ_0, 20 independent NVT MD simulations are conducted in the liquid basin, for a total of 1.357 ms , and 2,959 configurations are gathered at λ_1, separated by a minimum of 0.2 ns. The minimum number of crossings needed for computing transition probabilities at different λ's are given in Table S1.

The Origin of Large q_6 Values at the Interface

As depicted in Fig. 5*A* and Fig. S1*B*, $q_6(z)$ is surprisingly large at the free interface, despite the lack of any apparent crystalline order. This is due to the abundance of undercoordinated molecules at the interface. As can be seem in Fig. S6, q_6 histogram are shifted to the right for undercoordinated molecules. For single-coordinated molecules, in particular, the shift is considerable. Therefore, larger $q_6(z)$ values at the surface is not a reflection of higher crystallinity, but is instead due to the abundance of undercoordinated molecules.

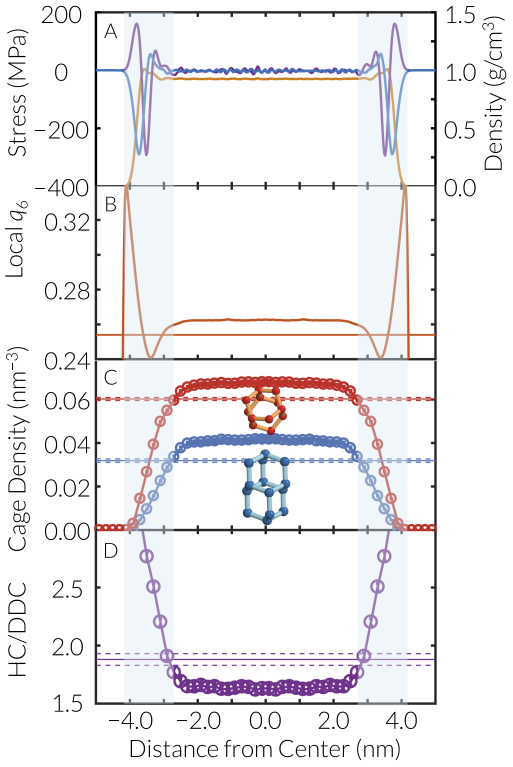

Fig. S1. Spatial profiles of density and normal and lateral stress (*A*), $q_6(z)$ (*B*), $\rho_{HC}(z)$ and $\rho_{DDC}(z)$ (*C*), and $\psi(z)$ (*D*) as a function of distance from the center of a 9-nm-thick TIP4P/ice film simulated at 230 K. The shaded blue region corresponds to the subsurface region as determined from anisotropy of the stress tensor. Neither of $q_6(z)$, $\rho_{HC}(z)$, $\rho_{DDC}(z)$ and $\psi(z)$ converge to the bulk values in the interior region of the 9-nm-thick film.

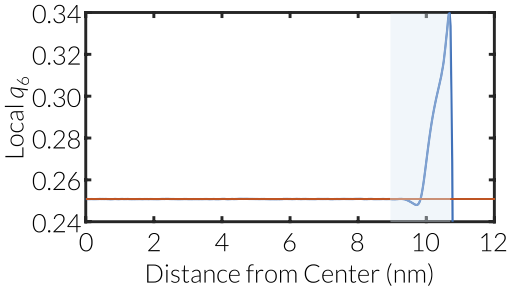

Fig. S2. Spatial profile of local q_6 in a 20-nm-thick mW film at 230 K. Unlike in TIP4P/ice, $q_6(z)$ converges to its respective bulk value in the interior region of the mW system, therefore behaving like thermodynamic quantities such as density and stress.

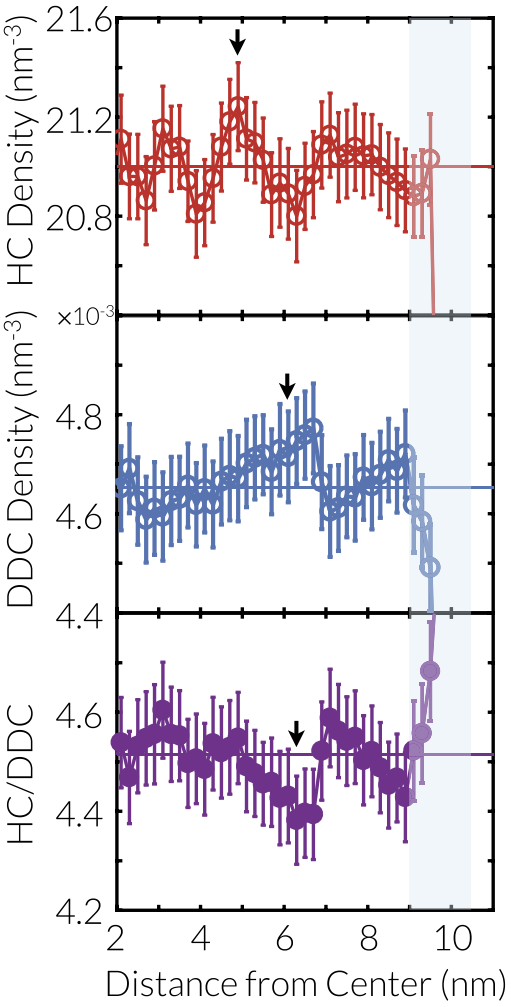

Fig. S3. Zoomed cage density and $\psi(z)$ profiles of Fig. 6. The shaded blue region corresponds to the 1.5-nm-thick subsurface region determined from the anisotropy of the stress tensor. For each profile, each arrow corresponds to the smallest z at which the deviation of the respective quantity from the bulk value, the horizontal line, exceeds the statistical uncertainty. This z value can be used to obtain a rough estimate of the decay length for each quantity, which is estimated to be 5.5, 4.5, and 4.5 nm for $\rho_{HC}(z)$, $\rho_{DDC}(z)$ and $\psi(z)$, respectively.

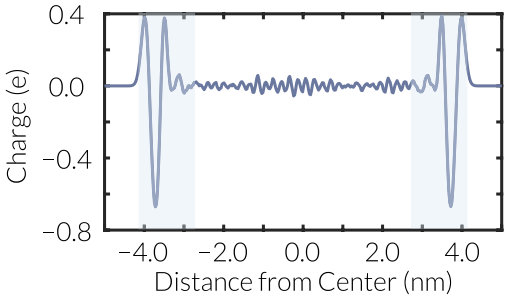

Fig. S4. Spatial profile of electrostatic charge across a 9-nm-thick TIP4P/ice film at 230 K. Note the lack of electrostatic neutrality in the shaded blue subsurface region, as determined from anisotropies of the stress tensor, similar to what has been reported in refs. 25 and 26 for the six-site model of ref. 24. However, freezing events initiate with electrostatically neutral interior regions of TIP4P/ice films.

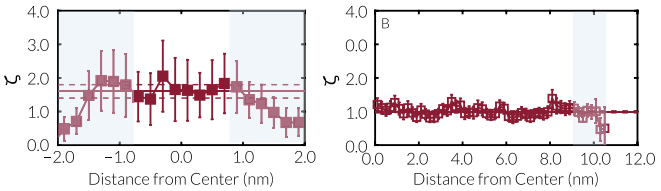

Fig. S5. Spatial profile of $\zeta(z)$ in a 4-nm-thick TIP4P/ice film at 230 K (*A*) and in a 20-nm-thick mW film at 230 K (*B*). Because of the scarcity of HC–HC connections, the error bars are much larger than the respective error bars in $\rho_{HC}(z)$, $\rho_{DDC}(z)$ and $\psi(z)$. The shaded blue regions denote the subsurface regions determined from the anisotropy of the stress tensor in the respective systems.

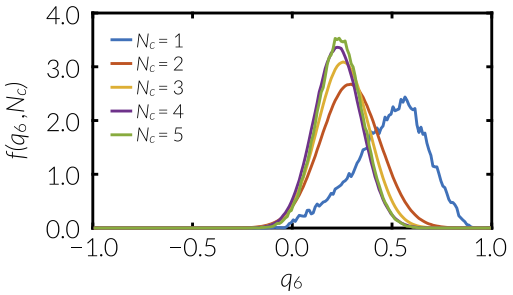

Fig. S6. Local q_6 distribution as a function of N_c, the number of molecules within the first nearest neighbor shell. Note that for single-coordinated molecules, the q_6 distribution is tilted toward the right, which explains the exceptionally high values of $q_6(z)$ at the vapor–liquid interface.

Table S1. Minimum number of crossings required for computing the transition probability at a given λ

λ Range	Minimum no. of crossings
12–37	4,000
44–54	2,000
66–80	600
96–440	275

Table S2. Simulation details for cage statistics calculations

Model	Geometry	N	Δt (fs)	t_{total} (μs)	N_{ind}
TIP4P/ice	Bulk	4,096	2.0	0.988	24
mW	Bulk	4,096	10.0	2.070	22
TIP4P/ice	Film, 4 nm	3,072	2.0	5.115	20
TIP4P/ice	Film, 9 nm	6,144	2.0	7.704	39
mW	Film	30,720	10.0	5.856	9

N is the system size, or the number of water molecules in the system. N_{ind} corresponds to the number of independent production runs conducted for each calculation, while t is the combined length of those N_{ind} simulations.